Angular Control of a Hybrid Magnetic Metamolecule Using Anisotropic FeCo

S. A. Gregory,[1] L. C. Maple,[1] G. B. G. Stenning,[2] T. Hesjedal,[3,*] G. van der Laan,[4] and G. J. Bowden[1]

[1]*School of Physics and Astronomy, University of Southampton, SO17 1BJ, United Kingdom*
[2]*ISIS Neutron and Muon Source, Rutherford Appleton Laboratory, Didcot OX11 0QX, United Kingdom*
[3]*Department of Physics, Clarendon Laboratory, University of Oxford, Oxford OX1 3PU, United Kingdom*
[4]*Magnetic Spectroscopy Group, Diamond Light Source, Didcot OX11 0DE, United Kingdom*

(Received 4 September 2015; published 25 November 2015)

By coupling magnetic elements to metamaterials, hybrid metamolecules can be created with useful properties such as photon-magnon mode mixing. Here, we present results for a split-ring resonator (SRR) placed in close proximity to a thin crystalline film of magnetically hard FeCo. Eddy-current shielding is suppressed by patterning the FeCo into 100-μm disks. At the ferromagnetic resonance (FMR) condition of FeCo, photon-magnon coupling strengths of 5% are observed. Altogether, three distinct features are presented and discussed: (i) remanent magnets allow FMR to be performed in a near-zero field, partially eliminating the need for applied fields; (ii) the anisotropic FMR permits angular control over hybrid SRR and FMR resonances; and (iii) the in-plane and out-of-plane magnetization of FeCo opens the door to "magnetically configurable metamaterials" in real time. Finally, a special study is presented of how best to excite the numerous transverse magnetic and electric modes of the SRR by using near-field excitation from a coplanar waveguide.

DOI: 10.1103/PhysRevApplied.4.054015

I. INTRODUCTION

Given the successful development of *passive* metamaterials with impressive applications, such as negative refractive index, invisibility cloaks, and superlenses [1,2], there has been a concerted effort in recent years to develop *active* metamaterials [3]. Such metamaterials can be controlled externally, allowing exploitation of functionalities in the time domain. For example, active metamaterials have been used (i) to enhance fast nonlinear switching [3] and (ii) to enhance luminescence in plasmonic quantum-dot metamaterials [4]. This work, in turn, has stimulated research into tunable hybrid metadevices which exploit microelectromechanical systems (MEMS), semiconductors, phase-change materials, liquid crystals, superconductors, and magnetic media [5–7]. In particular, magnetic materials have much to offer in the field of externally controllable nonlinear active metamaterials, given their inherent nonlinear magnetic behavior.

To date, research on magnetic-hybrid metamaterials has focused, primarily, on coupling Ohmic metamaterials, such as copper split-ring resonators (SRRs), with the ferromagnetic resonance (FMR) of ferrites [8–19]. In general, this work is performed largely by using magnetically isotropic ferrites such as yttrium iron garnet (YIG), notable for their widespread use in microwave electronics and low-loss magnetic resonance behavior [9,18,19]. In practice, the majority of experiments are carried out at relatively low frequencies of approximately 10 GHz by using cavity waveguides and bulk YIG single crystals [10,14,16]. An exception to this is the work reported in Refs. [9,20], which use coplanar waveguides (CPWs) to both excite the SRR and demonstrate magnetic control over the response of the SRR. Such planar device structures lend themselves to applications in microwave electronics [21–24].

However, YIG and other ferrites are restricted in their application because of their limited frequency range and/or high-magnetic-field demands. In addition, they are hard to either pattern or incorporate into multilayer structures. By contrast, the development of devices based on patterning metallic films has undergone a revolution over the past 25 years [25]. Metallic magnetic films can be easily patterned to micron or submicron length scales and incorporated into bilayers, multilayers, or magnetic spin-valve structures. In turn, this allows access to a rich variety of magnetic phenomena such as magnetic exchange bias [26], spintronics [27], magnetic vortex states in geometrically confined structures [28], Skyrmions [29], and the range of magnonic functionalities [30,31]. Of course, it should be acknowledged at the outset that high-frequency-induced eddy currents in the transition-metal films threaten to limit their use in active metadevices. However, if the transition-metal films are patterned into unconnected 100-μm disks, issues with eddy currents can be effectively negated. In particular, giant magnetic control (40 dB) has been demonstrated, over a SRR resonance at 17 GHz coupled to patterned disks of isotropic "permalloy" [20].

In this paper, we present results for a magnetic hybrid molecule, incorporating a hard FeCo film with remanent magnetic states. The thin film of single-crystalline FeCo is grown by molecular beam epitaxy (MBE) and subsequently

*Corresponding author.
Thorsten.Hesjedal@physics.ox.ac.uk

patterned into 100-μm disks. This allows two features to be demonstrated: (i) hard magnetic materials enable FMR to be performed in a zero or near-zero applied field, thus partially eliminating the need for strong applied fields; (ii) because the FMR is anisotropic, control over the angle of the hybrid metamolecule is achieved. As before, the advantages of a planar system are still maintained, i.e., device-ready and fully compatible with clean-room processes [20]. So, in principle, it should be possible to pattern such films for magnonic applications and hard-drive technologies.

Finally, we report a special study of how to excite the various transverse-magnetic (TM) and transverse-electric (TE) modes of the SRR, by using the *near-field* excitation of the CPW. By sliding a SRR over the transmission lines of the CPW, certain SRR modes are favored while others are suppressed. Such detail is important, if the strongest signal or modulation of a metamolecule resonance is to be achieved. In passing, we also note that physical movement of a SRR over a CPW enables MEM-like modulation of metamolecule resonances.

II. EXPERIMENTAL DETAILS

Much of the hardware used for the experiments reported here is already described in Refs. [9,20]. So only a minimalistic description is given here. A block schematic of the apparatus can be seen in Fig. 1.

The single-crystalline $Fe_{50}Co_{50}$ film is grown epitaxially on an MgO(001) substrate measuring 10×12 mm^2. A 3-nm-thick Fe seed layer is used to promote single-crystal growth of the 30-nm-thick $Fe_{50}Co_{50}$ film. The substrate is subsequently cut up into 5×5-mm^2 pieces for the experiment. The MBE growth procedure is identical to that for the FeCo film used in x-ray-detected FMR experiments described in Ref. [32]. The 30-nm-thick FeCo film is subsequently patterned into 100-μm disks, by using standard lithographic techniques in the clean-room facilities at the University of Southampton. An 8-μm-thick insulating SU-8 [33] layer is subsequently spun and cured on top of the FeCo disks. Next, a 300-nm-thick film of copper is deposited on top of the SU-8 layer and patterned into a SRR. Their proximity ensures excellent coupling between the FeCo disks and the SRR. The dimensions of the SRR are identical to those of Ref. [9]. Finally, a 1.3-μm-thin layer of photoresist is deposited on top of the SRR to provide insulation from the CPW. For the experiments, the FeCo and SRR stack is placed "flip-chip" on top of the CPW, as shown in Fig. 1. A schematic diagram of the stack, photograph, and SRR dimensions can be found in Sec. IV.

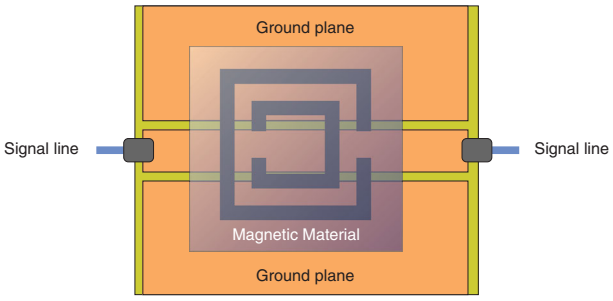

FIG. 1. The SRR (shown in black) is mounted on a grounded-plane CPW (yellow and orange). The magnetic FeCo patterned disks (not shown) are atop the SRR. This assembly is placed in an electromagnet providing magnetic fields of up to 0.9 T. A vector network analyzer (VNA) provides microwaves to the loaded CPW, in the frequency range 1–20 GHz. The VNA simultaneously measures the transmitted and reflected signals of the nominally 50Ω loaded CPW (the S parameters).

For the experiments, the CPW is connected to a VNA, which provides the microwave excitation while measuring the absorption or transmission properties of the loaded CPW in the form of the scattering matrix S. For the magnetic-field rotation experiments, the sample is placed in a portable octupole magnet system at the Diamond Light Source [34]. This magnet allows fields of up to 0.9 T to be applied in any direction. Thus, microwave transmission and reflection, the parameters S_{21} and S_{11}, respectively, can be measured as both a function of applied magnetic-field strength and orientation. The latter is important, because the FeCo FMR is strongly angle dependent, due to the fourfold magnetic anisotropy of the FeCo layer in the plane of the film.

Finally, it should be noted that the highly localized microwave-driving fields from the CPW and mutual coupling between the CPW and SRR are both strongly dependent on the relative position of the SRR with respect to the CPW transmission lines. Moreover, the SRR resonances are characterized by several TM and TE modes, all of which are strongly dependent on the near-field excitation of the CPW. Thus, if maximum signal or modulation is required, it is important to know which SRR mode is being excited and how to maximize it. Thus, prior to carrying out the experiments reported here, we decided to carry out a special study of the SRR modes of excitation, both experimentally and with finite-element simulations.

III. EXCITATION OF SRR TE AND TM MODES USING CPW EXCITATION

Foremost, it is important to appreciate that the strength of the electromagnetic (EM) fields generated by the CPW fall away very sharply with increasing distance from the CPW transmission lines. To examine this feature, numerical simulations of the "unloaded" CPW electric and magnetic fields are examined by using the finite-element package COMSOL v4.3b. Scattering boundary conditions are used as the simulation entrance and exit, and periodic boundary conditions are used as simulation walls. The minimum mesh element quality is above 0.1 (Ref. [35]). The results obtained at 10 GHz can be seen in Figs. 2(a) and 2(b). It is immediately obvious that the EM energy of the traveling wave is largely confined to the gaps in the

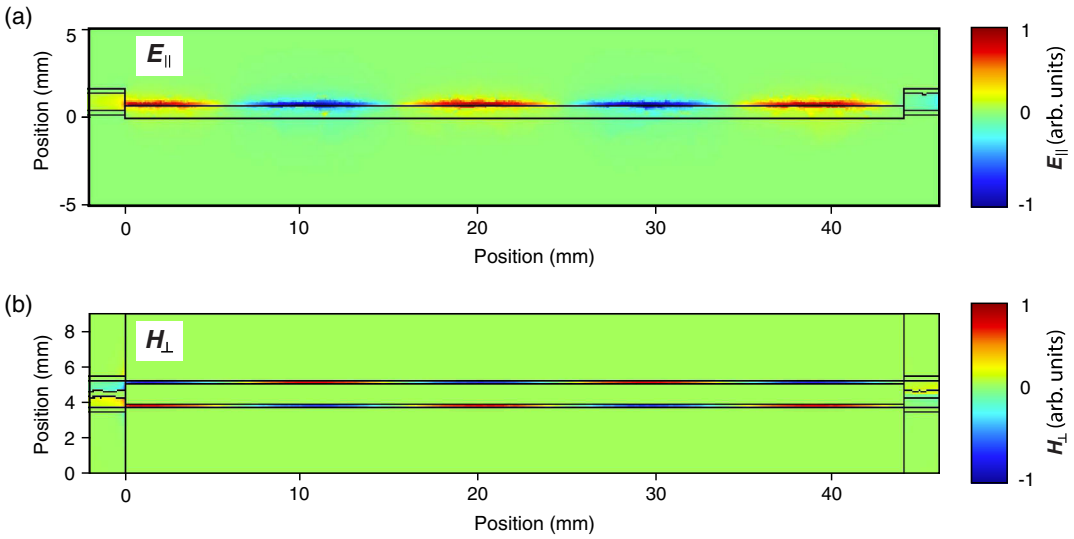

FIG. 2. Computer simulation, using COMSOL, of the electric- and magnetic-field distributions in the CPW. (a) Side view of the horizontal component of the electric field ($E_{\parallel}$) and (b) view from above of the vertical component of the magnetic field ($H_{\perp}$).

transmission lines of the CPW, with a wavelength along the CPW $\approx(2/3)\lambda_{\text{free space}}$. In particular, the EM fields at right angles to the CPW are highly localized, decaying rapidly on a length scale which is much smaller than the SRR size. In essence, therefore, FMR experiments performed by using CPW excitation can be described as "near-field excitation" [31,36]. To maximize the signal, it is therefore important to place both the SRR and FeCo disks as close as possible to the CPW transmission lines (in practice, micrometers, not millimeters).

Second, it is well known that the SRR resonances are characterized by several TE and TM modes of excitation [37–40]. For example, in free space, TM polarization excites magnetic modes and TE polarization excites electric modes [38]. Of course, the situation is more complicated when using near-field CPW excitation. The EM fields are highly localized around the signal line and gaps of the CPW. Thus, the system is highly spatially sensitive. In principle, it should be possible to simulate the effect of moving the SRR with respect to the CPW. However, in practice, this is difficult because (i) it is computationally expensive and (ii) technically challenging, due to a large variation in the mesh length scales (e.g., CPW length approximately 3 cm and SRR thickness approximately 300 nm), and (iii) there are difficulties in accounting for stray capacity. Of course, these disadvantages can be overcome by performing real-time experiments. We decided to physically move a SRR across the CPW transmission lines while simultaneously measuring the S parameters of the system. These translation experiments are performed by using a copper SRR patterned onto a glass plate, placed directly on a grounded CPW. The SRR is then pulled at right angles across the CPW by using a strip of acetate attached to a micrometer stage. A schematic representation of the experiment can be seen in Fig. 3(a). The resulting S_{21} scans, as a function of translation and frequency, are summarized in Fig. 3(c). This shows that, as the SRR is moved across the CPW transmission lines, several SRR resonances appear and disappear.

The resonances in Fig. 3(c) are labeled TM_o^1, TM_i^1, and TE_o^1, from left to right. The superscript 1 refers to "first" or lowest frequency mode. In practice, this "mode index" is defined by the number of current density nodes around the SRR [38]. However, the subscript indicates whether the mode is driven primarily by the outer ring (o) or inner ring (i) of the SRR [39,40]. In addition, our reasons for labeling the resonances in this way are also based on our simulations

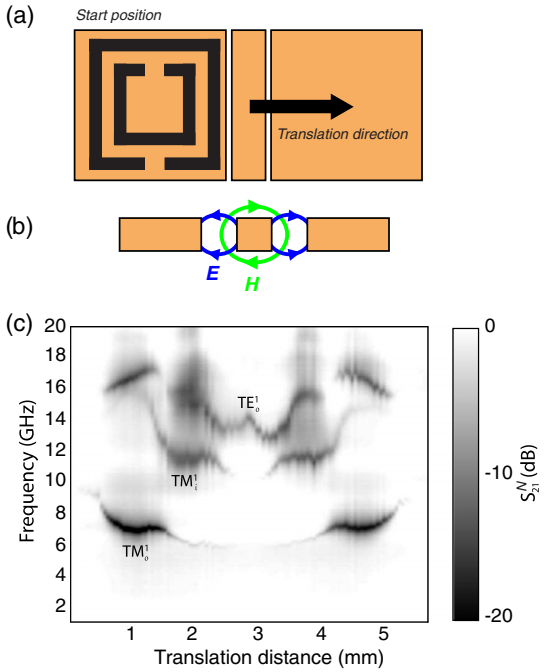

FIG. 3. (a) Top and (b) side view representations of the translation experiment, with the SRR at a position of 0 mm. (c) Map of S_{21}^N versus frequency and translation, in symmetric orientation. Three modes are clearly observable which wax, wane, and shift as the SRR is moved across the CPW.

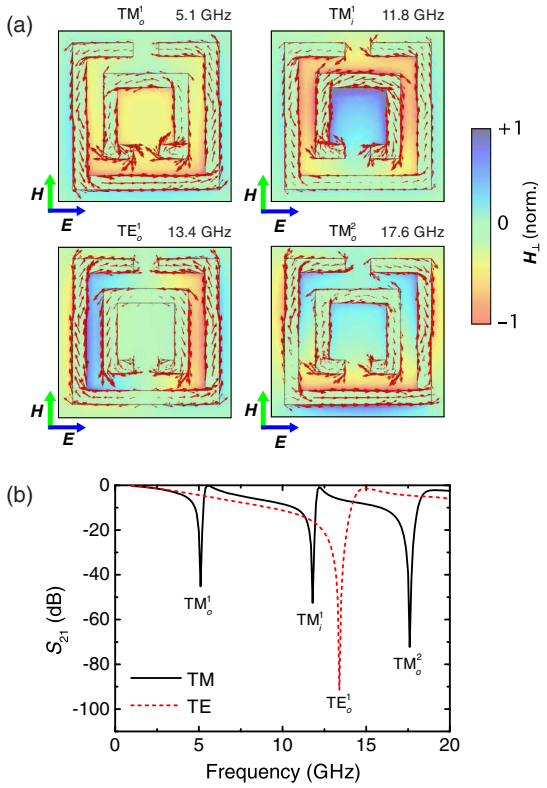

FIG. 4. (a) Computer-generated snapshots: the red arrows indicate currents, while the color shading shows the out-of-plane magnetic field. (b) The scattering parameter S_{21} versus frequency. This data is used to label the SRR resonances observed in Fig. 3.

summarized in Figs. 4(a) and 4(b). These are obtained by using finite-element simulations of a 2D infinite metamaterial of square SRRs sandwiched between FR4 [41] and glass. The SRR dimensions are identical to those used in the experiments, except that the thickness of the SRR is set at 0.3 mm, rather than 300 nm, to aid meshing. These computational results allow us to identify the nature of the SRR mode spectrum [see Fig. 4(a)] and take "snapshots" of the individual modes versus frequency [see Fig. 4(b)].

In practice, both the inner- and outer-ring excitations of the SRR resonances can be identified, with the latter occurring at a lower frequency [39,40]. It follows therefore that the lowest frequency mode appearing at approximately 7 GHz in Fig. 3(c) is the outer-ring-driven magnetic mode TM^1_o. The next two modes, appearing between 10 and 18 GHz, are the inner-ring-driven magnetic mode TM^1_i and outer-ring-driven electric mode TE^1_o, respectively. By symmetry, only TE modes are excited when the SRR is placed symmetrically over the center of the CPW, while the asymmetric TM modes are suppressed. These features are clearly evident in the experimental results presented in Fig. 3(c). Furthermore, the outer-ring modes appear earlier and disappear later than the inner-ring modes, because they are the first over the CPW signal line and the last to leave.

Finally, by using a grounded CPW rather than an ungrounded one, the (raw) transmission properties are improved and unwanted CPW resonances are suppressed.

IV. FeCo FMR RESULTS

As mentioned in Sec. II, the FeCo film is patterned into 100-μm disks to suppress eddy currents. Disks are chosen to negate any shape anisotropy in the plane of the film. Many more details of the FeCo and SRR stack, and its placement on the CPW, can be seen in Fig. 5.

For the experiments, the SRR is placed on the CPW with its center at about 1 mm from the center of the CPW to favor excitation of both TM^1_o and TE^1_o modes. Once in position, the sample is fixed to the CPW by using polytetrafluoroethylene tape. The loaded CPW, connected to the VNA, is subsequently placed within the octupole magnet. Prior to any measurements, the FeCo is saturated in a field of 0.3 T, in the desired direction, to ensure well-defined magnetic states. Also during the experiments, the CPW and microwave cables are not moved, since any shift in the cable position and/or connections alters the transmission and reflection properties measured by the VNA. The raw transmission S_{21} of the loaded CPW, as a function of frequency, in a zero field, can be seen in Fig. 6.

With this experimental arrangement, it is an easy matter to determine the FMR of the FeCo disks, as the magnetic field is rotated in the plane of the FeCo film. The results obtained in this way are summarized in Fig. 7.

The FMR data can be fitted by using the Kittel equations [42,43]. Explicitly,

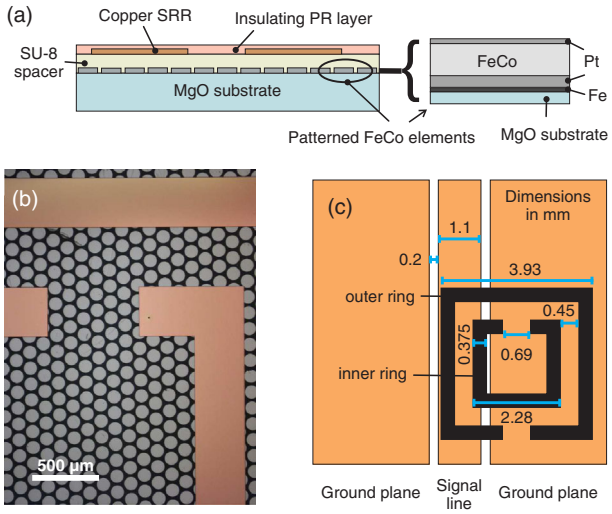

FIG. 5. (a) Schematic sample cross section of the multilayer sample showing the SRR and the patterned FeCo disks (not to scale). (b) Image of the sample through an optical microscope. (c) Placement of the SRR with respect to the CPW.

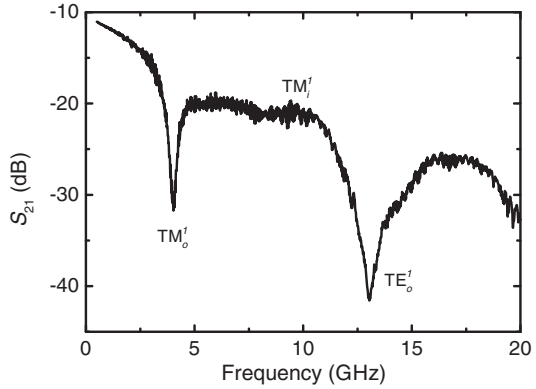

FIG. 6. The resonances of the SRR on the CPW at $B_a = 0$ T. The chosen geometry favors two modes: TM_o^1 at 4.03 GHz and TE_o^1 at 13.04 GHz. The TM_i^1 mode is also weakly excited but can only just be seen on this scale.

$$\nu = \gamma\sqrt{\mu_0 H_{\rm eff} B_{\rm eff}}, \tag{1a}$$

$$H_{\rm eff} = H\cos(\phi_M - \phi_H) + \frac{2K_C}{\mu_0 M_0}\cos 4(\phi_M - \phi_C) - \frac{2K_U}{\mu_0 M_0}\cos 2(\phi_M - \phi_U), \tag{1b}$$

$$B_{\rm eff} = \mu_0 H\cos(\phi_M - \phi_H) + \mu_0 M_0 + \frac{K_C}{2M_0}[3 + \cos 4(\phi_M - \phi_C)] - \frac{2K_U}{M_0}[1 + \cos 2(\phi_M - \phi_U)]. \tag{1c}$$

Here, ν is the frequency, and K_U and K_C are uniaxial and cubic anisotropy terms, respectively, while ϕ_M, ϕ_H, ϕ_U, and ϕ_C are the in-plane angles of magnetization, applied field, uniaxial, and cubic easy axis, respectively. All the other symbols possess their usual meanings. Following Ref. [32], Eqs. (1a)–(1c) can be simplified by (i) setting $\phi_M = \phi_H$ (valid in high magnetic fields) and (ii) assuming no uniaxial anisotropy, i.e., $K_U = 0$. Figure 7 shows the fitted FMR results versus the angle of applied field at 16 GHz, for both FeCo and the Fe seed layer. In doing so, we assume no coupling between the FeCo and Fe seed layers (see the discussion in Ref. [32]). The parameters for the FeCo film are found to be $\gamma = 29.4$ GHz T^{-1}, $M_0 = 1.72 \times 10^6$ A m^{-1}, $\phi_C = 45°$, and $K_C = 38.0$ kJ m^{-3}. The value of the cubic anisotropy parameter K_C lies between that found for the exchange-coupled bilayer $Ni_{81}Fe_{19}$(43.5 nm)/$Co_{50}Fe_{50}$(30 nm) of 32 kJ m^{-3} (Ref. [32]) and the bulk value of approximately 45 kJ m^{-3} (Ref. [44]). For the Fe seed layer, the gyromagnetic ratio γ and ϕ_C remain the same, while $M_0 = 1.15 \times 10^6$ A m^{-1} and $K_C = 13.4$ kJ m^{-3}. These values for the Fe saturation magnetization and the cubic anisotropy constant are quite different from bulk values but are consistent with similar thin Fe films on MgO given in Ref. [32].

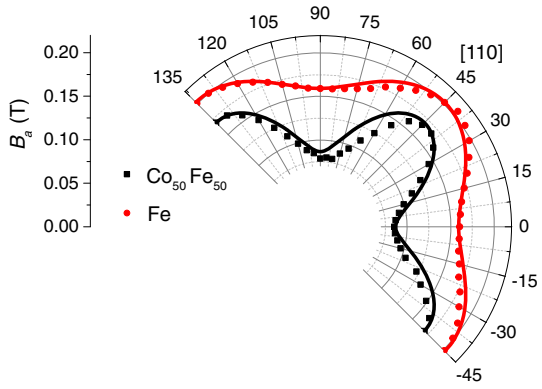

FIG. 7. FMR peak positions for the FeCo (black) and Fe seed (red) as a function of the applied field direction. The experimental FMR peak positions are determined by fitting Lorentz curves to the data. The solid lines are fits using Eq. (1). The Fe signal from the seed layer (3 nm) is very weak.

V. ANGULAR MODULATION OF SRR AND FMR ANTICROSSING

It has already been demonstrated, by using YIG and permalloy systems, that anticrossing occurs when the frequency of the FMR approaches that of the split-ring resonance [9,17,20]. However, unlike YIG and permalloy, the significant in-plane anisotropy of the FeCo means that the crossover field $B_{\rm co}$ (that field at which the FMR frequency equals that of a given SRR resonance) is now highly angle dependent. This feature is illustrated in Fig. 8, where the transmission parameter $S_{21}^N(\nu, B_a)$ can be seen for magnetic fields applied along the easy and hard directions, respectively. For example, for the TE_o^1 resonance at 13 GHz, FMR anticrossing occurs at ± 0.13 T (± 0.043 T) for fields applied along the easy (hard) axis, respectively. Thus, by simply rotating the magnetic field, the anticrossing for the TE_o^1 mode can be shifted between by about 0.1 T.

There are other features apparent in Fig. 8. For example, there is an additional anticrossing with the TM_o^1 mode at 4.0 GHz in Fig. 8(a). However, this anticrossing is absent in Fig. 8(b). The latter is forbidden, because the FMR frequency cannot drop below 8 GHz. Clearly, this particular anticrossing can be switched on and off simply by rotating the magnetic field through a few degrees. Also, the TM_i^1 mode is weakly excited at approximately 10 GHz and reveals anticrossing with the FMR. Finally, the faint FMR branch on the high-field side of the main magnetic resonance is that generated by the Fe seed layer. This, too, displays anticrossing behavior, despite being (i) only 3 nm thick and (ii) shielded by the FeCo layer, which lies between it and the CPW.

It is possible to fit the data of Fig. 8, by using a simple extension to the two-level oscillator model used to describe

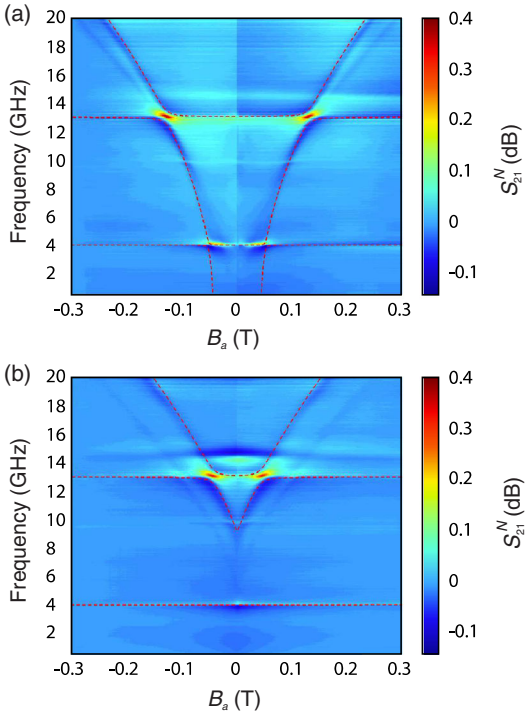

FIG. 8. Map of $S_{21}^N(\nu, B_a)$ for frequency versus magnetic field, with the magnetic field applied along the (a) easy axis (0°) and (b) hard axis (45°) of the FeCo. The raw S_{21} data is "normalized" to a scan taken at 0.3 T, where the FMR is beyond the available frequency range. Dashed lines are fit by using a four-level coupled oscillator model.

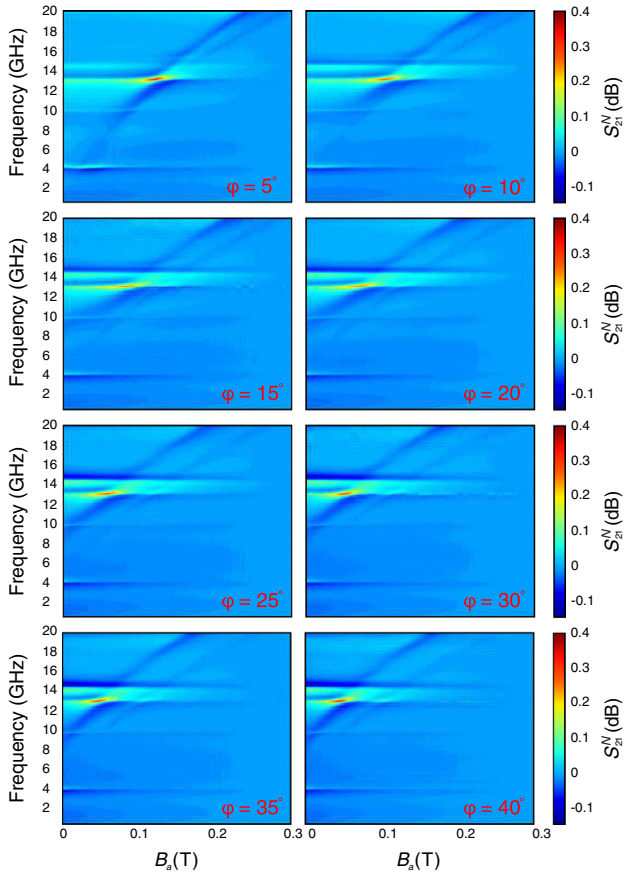

FIG. 9. Maps of $S_{21}^N(\nu, B_a)$ obtained at 5° steps between the easy and hard axes.

anticrossing behavior between SRR and FMR modes, in a soft magnetic material [9,17,20]. Given two principle SRR modes, it is necessary to use a four-level coupled oscillator model. We write

$$\nu_1^{\pm} = \frac{\nu_{\mathrm{FMR}} + \nu_{\mathrm{SRR},1}}{2} \pm \sqrt{\left(\frac{\nu_{\mathrm{FMR}} - \nu_{\mathrm{SRR},1}}{2}\right)^2 + \Delta_1^2}, \tag{2a}$$

$$\nu_2^{\pm} = \frac{\nu_1^{+} + \nu_{\mathrm{SRR},2}}{2} \pm \sqrt{\left(\frac{\nu_1^{+} - \nu_{\mathrm{SRR},2}}{2}\right)^2 + \Delta_2^2}. \tag{2b}$$

Here Δ_1 (Δ_2) details the strength of the mutual interaction (in gigahertz) between the SRR resonances $\nu_{\mathrm{SRR},1}$ ($\nu_{\mathrm{SRR},2}$), respectively, with the FeCo FMR resonance ν_{FMR}. Note that the ν_1^+ branch is essentially the FMR line sweeping up to meet the second SRR resonance.

The dashed lines in Fig. 8 represent a fit to the experimental data, obtained by using Eqs. (1a) and (2b). The SRR resonance and splitting parameters are found to be $\nu_{\mathrm{SRR},1} = 4.0$ GHz and $\nu_{\mathrm{SRR},2} = 13.0$ GHz, respectively, in agreement with the results presented in Fig. 6. The mutual SRR and FMR interaction parameters are found to be $\Delta_{\mathrm{SRR},1} = 0.2$ GHz and $\Delta_{\mathrm{SRR},2} = 0.4$ GHz, respectively. These values for Δ are very similar to those of Ref. [20]. However, it should be noted that the model does not take into account (i) the linewidth of the resonances involved and (ii) broadening due to the formation of magnetic domains, particularly at low magnetic fields.

Finally, the full angular switching between the easy and hard magnetization directions can be seen in Fig. 9. At intermediate angles, the amount of modulation of the split-ring resonance is reduced by approximately 25%, due to the rotation of the FeCo magnetization away from a preferred axis.

VI. RESULTS FOR AN ASYMMETRIC ORIENTATION OF SRR TO CPW

In addition to the $S_{21}^N(\nu, B_a)$ maps described in Sec. V, many more are obtained both for differing positions and rotations of the SRR with respect to the CPW and for patterned permalloy films. One such result, for the patterned permalloy film, can be seen in Fig. 10. Here the SRR is rotated by 90° and placed at a displacement of 3.75 mm with respect to the center of the CPW. Both sample geometries are identical, except for the replacement of the FeCo with permalloy [20].

Figure 10 can be used to illustrate two points. The first point to note is the differences in the strength of the S_{21}^N signal between the FeCo (Figs. 8 and 9) and that obtained

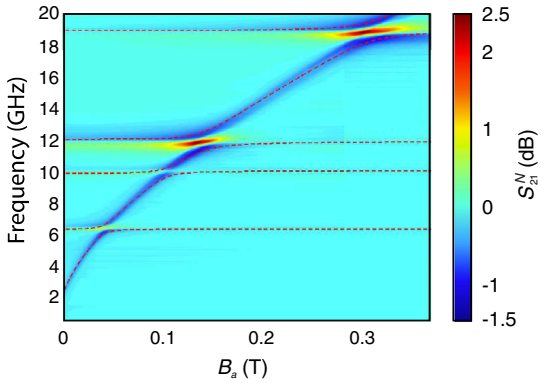

FIG. 10. Map of $S^N_{21}(\nu, B_a)$ showing four distinct SRR and FMR anticrossings, this time obtained by using patterned permalloy disks. The red dashed lines represent a fit to the data using an eight-level coupled oscillator model.

with permalloy (Fig. 10). The signal obtained by using permalloy is some 10 times stronger that of the FeCo. Clearly, the mutual interaction between the SRR and FMR modes is much stronger when high-permeability permalloy is used. Some of the difference can probably be attributed to the difference in thickness of the two films in question ($Ni_{81}Fe_{19}$, 150 nm thick, and $Fe_{50}Co_{50}$, 30 nm thick). However, one way of increasing the mutual interaction between the SRR and the FeCo film would be to decrease the distance of the SU-8 insulating layer below 8 μm. Second, the identification of the various SRR modes is made in the same way as that described in Sec. III and is not detailed here. What we wish to highlight is how well the extended multicoupled model oscillator can be used to describe multiple anticrossings. A fit to the data, using an eight-level coupled oscillator model, is represented by the red dotted lines in Fig. 10. The model parameters obtained in this way are listed in Table I.

It is clear that the fit to the observed $S^N_{21}(\nu, B_a)$ data is excellent, allowing measurements of the coupling strength between the SRR and FMR modes. In particular, it is the TM^1 modes which give the highest relative splitting $k = \Delta/\nu_{SRR}$, as found by Ref. [17]. Finally, the model yields details of the hybridization of the SRR modes with FMR, at every frequency and field in the $S^N_{21}(\nu, B_a)$ map. Of course, at the precise center of an anticrossing, the upper and lower modes are characterized by 50% SRR and 50% FMR. Such mode mixing may well have applications for coherent information transfer in microwave quantum devices which exploit strong coupling between magnons and microwave photons, as discussed, for example, in Refs. [17,45–48].

TABLE I. The parameters obtained by using an eight-level coupled oscillator model fit to the data shown in Fig. 10. The separation at a given anticrossing is 2Δ.

ν_{SRR} (GHz)	Mode	Δ (GHz)	Coupling strength (Δ/ν_{SRR})
6.7	TM^1_o	0.3	4.5%
10.3	TE^1_o	0.4	3.9%
12.1	TM^1_i	0.62	5.1%
18.9	TM^2_o	0.69	3.65%

VII. DISCUSSION AND CONCLUSIONS

Results are presented for a magnetic hybrid metamolecule, involving a SRR placed in close proximity to a magnetically hard thin FeCo film. To suppress eddy-current shielding, the FeCo film is patterned into 100-μm disks. Two features are demonstrated: (i) hard magnetic materials enable FMR and can be performed in zero or near-zero applied fields, thus partially eliminating the need for an applied field; (ii) because the FMR is anisotropic, angular control over metamolecule hybrid resonances is achieved. Simply by rotating the magnetic field, the crossover field B_{co} at a given anticrossing can be varied from 0.04 to 0.13 T. This degree of control is much larger than that which can be obtained by sweeping across a single anticrossing [20]. In addition, a special study is reported on the effect of the near-field CPW excitation on SRR resonances. Here, both the character and strength of the signal depend strongly on the relative position of the SRR with respect to the CPW. In particular, it is shown how to identify and optimize the various TM and TE modes of the SRR, by using near-field CPW excitation. Such detail is important, if the strongest signal or modulation of a metamolecule resonance is to be achieved.

It is also worth noting that the use of hard materials, with remanent magnetization, opens the door to magnetically reconfigurable metamaterials in the time domain. For example, the resolution of magnetic switching in hard-drive technology is of the order of 10 nm. Such a resolution is more than enough for local switching of the FeCo magnetic disks above the SRR. So we have the possibility of manipulating the SRR and FeCo magnetic coupling in a time-sequential fashion. For example, the near-field maps of Fig. 4(a) show the simulated out-of-plane magnetic-field components for the first four modes of the SRR. These fields compete with the out-of-plane component of the FMR, and it this competition which gives rise to anticrossing behavior. However, in a magnetically configurable metamaterial, the magnetization of the FeCo disks can be realigned, allowing the SRR and FMR coupling to be modified in the time domain. For example, in the TM^1_i mode at 11.8 GHz [see Fig. 4(a), top left], the fields in the SRR gaps are both pointing down (both shaded orange). However, in the TE^1_i mode at 13.4 GHz, the two fields in question are pointing in opposite directions (one shaded blue, one shaded orange). So by switching the magnetization of the FeCo disks above the two gaps, from in plane to out of plane, SRR and FMR hybridization of these modes can be switched on and off. Such detailed considerations

can also be used to point the way to improving photon-magnon coupling. First, the COMSOL data in Fig. 4 shows that the out-of-plane microwave fields are strongest above the gaps in the SRR. So if we wish to promote phase-coherent SRR and FMR coupling, the patterned FeCo disks should be placed directly over the SRR gaps and nowhere else. Second, it should be possible to increase the quality factor of a particular SRR mode, either by intelligent design and/or by going to lower temperatures.

Finally, it is demonstrated that the simple two-level SRR and FMR oscillator model, developed to explain a single anticrossing [17,20], can be very successfully extended to deal with the numerous TM and TE modes of a SRR coupled to a ferromagnetic film.

ACKNOWLEDGMENTS

We acknowledge Diamond Light Source for time on beam line I10 under Proposal No. SI-10152. S. A. G. gratefully acknowledges funding by the Defence and Security Ph.D. programme managed by the Defence Science and Technology Laboratory (Dstl). We thank Adriana Figueroa for help with VNA measurements at Diamond.

[1] D. R. Smith, J. B. Pendry, and M. C. K. Wiltshire, Metamaterials and negative refractive index, Science **305**, 788 (2004).
[2] T. Xu, A. Agrawal, M. Abashin, K. J. Chau, and H. J. Lezec, All-angle negative refraction and active flat lensing of ultraviolet light, Nature (London) **497**, 470 (2013).
[3] N. I. Zheludev and Y. S. Kivshar, From metamaterials to metadevices, Nat. Mater. **11**, 917 (2012).
[4] K. Tanaka, E. Plum, J. Y. Ou, T. Uchino, and N. I. Zheludev, Multifold Enhancement of Quantum Dot Luminescence in Plasmonic Metamaterials, Phys. Rev. Lett. **105**, 227403 (2010).
[5] O. Hess, J. B. Pendry, S. A. Maier, R. F. Oulton, J. M. Hamm, and K. L. Tsakmakidis, Active nanoplasmonic metamaterials, Nat. Mater. **11**, 573 (2012).
[6] J. Zhou, D. R. Chowdhury, R. Zhao, A. K. Azad, H.-T. Chen, C. M. Soukoulis, A. J. Taylor, and J. F. O'Hara, Terahertz chiral metamaterials with giant and dynamically tunable optical activity, Phys. Rev. B **86**, 035448 (2012).
[7] S. Zhang, J. Zhou, Y.-S. Park, J. Rho, R. Singh, S. Nam, A. K. Azad, H.-T. Chen, X. Yin, A. J. Taylor, and X. Zhang, Photoinduced handedness switching in terahertz chiral metamolecules, Nat. Commun. **3**, 942 (2012).
[8] Y.-J. Yang, Y.-J. Huang, G.-J. Wen, J.-P. Zhong, H.-B. Sun, and O. Gordon, Tunable broadband metamaterial absorber consisting of ferrite slabs and a copper wire, Chin. Phys. B **21**, 038501 (2012).
[9] G. B. G. Stenning, G. J. Bowden, L. Maple, S. A. Gregory, A. Sposito, R. W. Eason, N. I. Zheludev, and P. A. J. de Groot, Magnetic control of a meta-molecule, Opt. Express **21**, 1456 (2013).
[10] L. Kang, Q. Zhao, H. Zhao, and J. Zhou, Magnetically tunable negative permeability metamaterial composed by split ring resonators and ferrite rods, Opt. Express **16**, 8825 (2008).
[11] Y. J. Huang, G. J. Wen, Y. J. Yang, and K. Xie, Tunable dual-band ferrite-based metamaterials with dual negative refractions, Appl. Phys. A **106**, 79 (2012).
[12] H. Zhao, J. Zhou, Q. Zhao, B. Li, L. Kang, and Y. Bai, Magnetotunable left-handed material consisting of yttrium iron garnet slab and metallic wires, Appl. Phys. Lett. **91**, 131107 (2007).
[13] J. N. Gollub, J. Y. Chin, T. J. Cui, and D. R. Smith, Hybrid resonant phenomena in a SRR/YIG metamaterial structure, Opt. Express **17**, 2122 (2009).
[14] K. Bi, J. Zhou, H. Zhao, X. Liu, and C. Lan, Tunable dual-band negative refractive index in ferrite-based metamaterials, Opt. Express **21**, 10746 (2013).
[15] J. Ghalibafan, N. Komjani, and B. Rejaei, Design and analysis of a novel tunable ferrite based left handed strip line, J. Electromagn. Waves Appl. **26**, 914 (2012).
[16] Y. Huang, G. Wen, T. Li, and K. Xie, Low-loss, broadband and tunable negative refractive index metamaterial, J. Electromagn. Anal. Appl. **02**, 104 (2010).
[17] B. Bhoi, T. Cliff, I. S. Maksymov, M. Kostylev, R. Aiyar, N. Venkataramani, S. Prasad, and R. L. Stamps, Study of photon-magnon coupling in a YIG-film split-ring resonant system, J. Appl. Phys. **116**, 243906 (2014).
[18] G. P. Rodrigue, A generation of microwave ferrite devices, Proc. IEEE **76**, 121 (1988).
[19] V. G. Harris, A. Geiler, Y. Chen, S. D. Yoon, M. Wu, A. Yang, Z. Chen, P. He, P. V. Parimi, X. Zuo, C. E. Patton, M. Abe, O. Acher, and C. Vittoria, Recent advances in processing and applications of microwave ferrites, J. Magn. Magn. Mater. **321**, 2035 (2009).
[20] S. A. Gregory, G. B. G. Stenning, G. J. Bowden, N. I. Zheludev, and P. A. J. de Groot, Giant magnetic modulation of a planar, hybrid metamolecule resonance, New J. Phys. **16**, 063002 (2014).
[21] F. Martin, F. Falcone, J. Bonache, R. Marques, and M. Sorolla, Miniaturized coplanar waveguide stop band filters based on multiple tuned split ring resonators, IEEE Microwave Compon. Lett. **13**, 511 (2003).
[22] F. Martin, J. Bonache, F. Falcone, M. Sorolla, and R. Marques, Split ring resonator based left-handed coplanar waveguide, Appl. Phys. Lett. **83**, 4652 (2003).
[23] F. Falcone, F. Martin, J. Bonache, R. Marques, and M. Sorolla, Coplanar waveguide structures loaded with split-ring resonators, Microwave Opt. Technol. Lett. **40**, 3 (2004).
[24] I. Gil, J. Bonache, J. Garcia-Garcia, and F. Martin, Tunable metamaterial transmission lines based on varactor-loaded split-ring resonators, IEEE Trans. Microwave Theory Tech. **54**, 2665 (2006).
[25] M. Geissler and Y. Xia, Patterning: Principles and some new developments, Adv. Mater. **16**, 1249 (2004).
[26] J. Stöhr and H. C. Siegmann, *Magnetism* (Springer-Verlag Berlin, Heidelberg, 2006).
[27] F. Pulizzi, Spintronics, Nat. Mater. **11**, 367 (2012).
[28] V. Novosad, F. Y. Fradin, P. E. Roy, K. S. Buchanan, K. Yu. Guslienko, and S. D. Bader, Magnetic vortex resonance in patterned ferromagnetic dots, Phys. Rev. B **72**, 024455 (2005).

[29] A. Fert, V. Cros, and J. Sampaio, Skyrmions on the track, Nat. Nanotechnol. **8**, 152 (2013).
[30] B. Lenk, H. Ulrichs, F. Garbs, and M. Münzenberg, The building blocks of magnonics, Phys. Rep. **507**, 107 (2011).
[31] V. V. Kruglyak, S. O. Demokritov, and D. Grundler, Magnonics, J. Phys. D **43**, 264001 (2010).
[32] G. B. G. Stenning, L. R. Shelford, S. A. Cavill, F. Hoffmann, M. Haertinger, T. Hesjedal, G. Woltersdorf, G. J. Bowden, S. A. Gregory, C. H. Back, P. A. J. de Groot, and G. van der Laan, Magnetization dynamics in an exchange-coupled NiFe/FeCo bilayer studied by x-ray detected ferromagnetic resonance, New J. Phys. **17**, 013019 (2015).
[33] MicroChem SU-8 permanent epoxy negative photoresist, http://www.microchem.com/Prod-SU83000.htm.
[34] G. van der Laan and A. I. Figueroa, X-ray magnetic circular dichroism—A versatile tool to study magnetism, Coord. Chem. Rev. **277–278**, 95 (2014).
[35] Size parameters for free tetrahedral meshing in COMSOL multiphysics, https://www.comsol.com/blogs/size-parameters-free-tetrahedral-meshing-comsol-multiphysics/.
[36] R. N. Simons, *Coplanar Waveguide Circuits, Components & Systems* (Wiley, New York, 2004).
[37] J. D. Baena, J. Bonache, F. Martin, R. M. Sillero, F. Falcone, T. Lopetegi, M. A. G. Laso, J. Garcia-Garcia, I. Gil, M. F. Portillo, and M. Sorolla, Equivalent-circuit models for split-ring resonators and complementary split-ring resonators coupled to planar transmission lines, IEEE Trans. Microwave Theory Tech. **53**, 1451 (2005).
[38] J. Zhou, T. Koschny, and C. M. Soukoulis, Magnetic and electric excitations in split ring resonators, Opt. Express **15**, 17881 (2007).
[39] N. Liu, H. Guo, L. Fu, H. Schweizer, S. Kaiser, and H. Giessen, Electromagnetic resonances in single and double split-ring resonator metamaterials in the near infrared spectral region, Phys. Status Solidi B **244**, 1251 (2007).
[40] H. Guo, N. Liu, L. Fu, T. P. Meyrath, T. Zentgraf, H. Schweizer, and H. Giessen, Resonance hybridization in double split-ring resonator metamaterials, Opt. Express **15**, 12095 (2007).
[41] Glass-reinforced epoxy laminate sheets, http://www.farnell.com/datasheets/1644697.pdf.
[42] C. Kittel, On the theory of ferromagnetic resonance absorption, Phys. Rev. **73**, 155 (1948).
[43] M. Farle, Ferromagnetic resonance of ultrathin metallic layers, Rep. Prog. Phys. **61**, 755 (1998).
[44] T. Kuschel, J. Hamrle, J. Pistora, K. Saito, S. Bosu, Y. Sakuraba, K. Takanashi, and J. Wollschläger, Magnetic characterization of thin $Co_{50}Fe_{50}$ films by magnetooptic Kerr effect, J. Phys. D **45**, 495002 (2012).
[45] H. Huebl, C. W. Zollitsch, J. Lotze, F. Hocke, M. Greifenstein, A. Marx, R. Gross, and S. T. B. Goennenwein, High Cooperativity in Coupled Microwave Resonator Ferrimagnetic Insulator Hybrids, Phys. Rev. Lett. **111**, 127003 (2013).
[46] Y. Tabuchi, S. Ishino, T. Ishikawa, R. Yamazaki, K. Usami, and Y. Nakamura, Hybridizing Ferromagnetic Magnons and Microwave Photons in the Quantum Limit, Phys. Rev. Lett. **113**, 083603 (2014).
[47] X. Zhang, C. L. Zou, L. Jiang, and H. X. Tang, Strongly Coupled Magnons and Cavity Microwave Photons, Phys. Rev. Lett. **113**, 156401 (2014).
[48] G. Kurizki, P. Bertet, Y. Kubo, K. Mølmer, D. Petrosyan, P. Rabl, and J. Schmiedmayer, Quantum technologies with hybrid systems, Proc. Natl. Acad. Sci. U.S.A. **112**, 3866 (2015).